Research Article

Ambreen Afridi*, Sumama Nuthana Kalva, Ans Al Rashid, Noor A. Al-Maslamani, and Muammer Koç

Magnesium-reinforced PMMA composite scaffolds: Synthesis, characterization, and 3D printing *via* stereolithography

https://doi.org/10.1515/ntrev-2025-0195
received February 12, 2025; accepted June 6, 2025

Abstract: Metal particle-reinforced polymer resin scaffolds are becoming increasingly prominent in biomedical applications due to their potential to support tissue regeneration and healing. These scaffolds are designed to serve as temporary frameworks that support affected tissues and gradually degrade during healing. The primary focus of these research efforts has been on determining the optimal materials and methods for creating these scaffolds, ensuring that they are biocompatible, capable of withstanding structural strains, and can support cellular proliferation, tissue growth, and vascularization. Despite the growing interest in polymers and their metal composites, a notable gap exists in leveraging the benefits of fabricating these composites through additive manufacturing techniques, particularly stereolithography (SLA). Magnesium (Mg), in particular, is a biocompatible and osteoconductive material known for its remarkable mechanical properties and biodegradability, making it highly suitable for bone implants. Additionally, Mg can potentially regenerate skin tissues and inhibit bacterial infections. Mg ions are crucial for wound healing because they repair the skin barrier and facilitate blood coagulation. This research focuses on finding optimal conditions for manufacturing magnesium-induced poly(methyl methacrylate) (PMMA) resin scaffolds using SLA. To evaluate their printability and the effect of different material compositions on the 3D-printed structures, PMMA resin was mixed with high-weight percentages (wt%) of Mg alloy WE43. This mixture was then used to 3D-print test coupons and scaffolds *via* SLA. The impact of Mg incorporation on the scaffold's structural integrity, thermal degradation, and biological response was assessed through physicochemical and thermal characterization and biocompatibility experiments. Notably, pure PMMA exhibited the highest tensile strength, 26.23 ± 0.14 MPa and an elastic modulus of 707.81 MPa, while PMMA resin/1% Mg showed the lowest strength (19.46 ± 0.25 MPa) and modulus (392.88 MPa), indicating a decrease in mechanical integrity with higher Mg content. However, the thermal stability was enhanced with the addition of Mg as the thermal degradation onset improved from ~310 to 335°C. The challenges encountered in manufacturing PMMA resin/Mg composites and their potential applications were discussed, highlighting the future directions and promising avenues for further research and development.

Keywords: stereolithography, magnesium-reinforced PMMA, 3D-printed scaffolds, bone tissue engineering, magnesium biocomposites, biocompatibility, additive manufacturing, porous biomaterials

1 Introduction

The fast-evolving field of biomedical engineering demands innovative materials and manufacturing techniques to tackle growing challenges. Biomaterials, including ceramics, polymers, metals, and composites, are instrumental in diagnosis, therapy, tissue repair and replacement, and enhancing the function of biological systems [1]. They are crucial for orthoedic and dental implants, bone plates, prosthetic joints, screws, rods, load-bearing components, and cardiovascular stents. These materials offer a unique blend of strength, energy absorption, flexibility, biocompatibility, and biodegradability [2,3]. Additionally, they are cost-effective and customizable and can be designed on demand [4,5]. One of the critical aspects of tissue engineering is creating scaffolds that closely resemble the extracellular matrix of natural tissues in terms of their intricate architecture and design [6]. The scaffolds must enhance structural stability, promote cell adhesion and proliferation, and degrade at a rate consistent with natural

*** Corresponding author: Ambreen Afridi,** Division of Sustainable Development, College of Science and Engineering, Hamad Bin Khalifa University, Qatar Foundation, Doha, 34110, Qatar,
e-mail: amaf64803@hbku.edu.qa, afridiamber08@gmail.com
Sumama Nuthana Kalva, Ans Al Rashid, Muammer Koç: Division of Sustainable Development, College of Science and Engineering, Hamad Bin Khalifa University, Qatar Foundation, Doha, 34110, Qatar
Noor A. Al-Maslamani: Qatar Biomedical Research Institute, Hamad Bin Khalifa University, Qatar Foundation, Doha, 34110, Qatar

tissue regeneration [7,8]. Notably, integrating mechanical optimization [9], structural tunability [10], and piezoelectric functionality [11] into the scaffold enables it to provide mechanical support, adapt to bone defects, and generate electrical signals to stimulate healing, making it highly effective for complex tissue repair.

For tissue engineering applications, metals and metallic alloys, including titanium, stainless steel, and Co–Cr alloys, are widely accessible implants due to their exceptional mechanical strength, biocompatibility, and corrosion resistance properties [12–14]. However, the disparity in elastic moduli between bone and metal results in stress shielding, impeding the healing process. These materials do not degrade over time, necessitating a subsequent surgical procedure to remove the implants [15]. Alternatively, biodegradable metals gradually dissolve within the human body and have emerged as promising replacements for traditional permanent implants [16]. Biodegradable materials can be categorized into pure metals, alloys, and metal matrix composites. Their properties, such as tensile strength, yield strength, Young's modulus, and corrosion resistance, can be customized by incorporating reinforcements [17,18]. To harness these properties, various fabrication techniques – including casting, powder metallurgy, and additive manufacturing (AM) – are being developed to produce structures with tailored structural and biological performance [19,20]. Iron, zinc, and magnesium (Mg), and their respective alloys, are the key reinforcements for biomedical applications [21–23]. Iron alloys exhibit high strength but have a slow degradation rate that can lead to stress concentrations [21]. Zinc alloys, while having an acceptable degradation rate, suffer from inadequate mechanical properties [22]. In contrast, Mg, the fourth most abundant element in the human body [17], stands out as a superior candidate due to its being a biocompatible material [16,24] with osteoconductive [3] and antimicrobial properties, making it ideal for bone implants and wound healing applications [25,26].

Despite these advantages, conventional manufacturing of composites often falls short of producing intricate and precise magnesium-based implants that perfectly mimic the complex structures of the human body [7,8,15]. Hence, there has been an increasing interest in developing 3D-printable Mg-polymer composites through AM, as they are promising alternatives for biomedical or pharmaceutical products [18]. AM, or three-dimensional printing (3DP), is a rapid prototyping technique that has revolutionized the manufacturing industry [27] by enabling precise control over material properties, including porosity, functional groups, roughness, degradability, and drug release profile [28]. Incorporating AM technologies into the pharmaceutical industry and tissue engineering allows for the production of high-quality, personalized, and intricate structures, decreases production costs, and enhances patient adherence [29–31]. It also advances transdermal and topical drug delivery systems like microneedles and patches, offering non-invasive, user-friendly alternatives to oral administration [32–37]. Among AM techniques, stereolithography (SLA) stands out for its high resolution and surface quality [38,39]. Based on the principle of photopolymerization, SLA uses a UV laser to cure photosensitive resin layer by layer [40]. The photopolymer resin consists of precursors (monomers or oligomers), photoinitiators, binders, chain transfer agents, absorbers, and additives [41–43]. SLA enables the fabrication of intricate structures with resolutions up to 10 μm [44,45], across a broad size range, from submicron to decimeter scales [42,46]. Its precision and surface quality surpass other low-cost 3DP methods, making it especially valuable in biomedical applications such as patient-specific implants, surgical tools, hearing aids, and innovative drug delivery systems [47,48].

Studies have shown that Mg-polymer composites promote attachment, proliferation, and differentiation of various cells [49] while also stimulating bone regeneration in animal models [18,23,50]. Their magnesium content influences biocompatibility, mechanical properties, and degradation. With controlled porosity and strength, these composites enable the fabrication of customized bone scaffolds ideal for tissue regeneration [51–53]. Tsai *et al.* [54] produced 3D-printed porous bioactive scaffolds by incorporating magnesium-calcium silicate (Mg–CS) powder with poly-ε-caprolactone (PCL). The Mg-CS content strongly enhanced the bone development in simulated body fluid. The biocompatibility of scaffolds was verified through *in vitro* experiments utilizing human mesenchymal stem cells (hMSCs). Dong *et al.* [55] introduced a room-temperature extrusion-based AM method to create porous Mg scaffolds. Rheological and thermal analyses were performed for the samples with 54, 58, and 62% Mg powder. The printed scaffolds featured interconnected hierarchical pores and showed high porosity. Another study by Lin *et al.* [56] utilized 3D gel printing (3DGP) technology to fabricate porous Mg scaffolds. They mixed Mg powder with a premixed epoxy resin and ethanol solution to form a printable slurry. After printing, the samples underwent debinding and sintering processes. The scaffolds were implanted into the femoral condyles of rats and monitored for five weeks. The greatest compressive strength of the Mg scaffolds was attained at 64.4% porosity after sintering at 610°C. The study found that Mg scaffolds coated with oxide exhibited good degradability and biocompatibility. Kalva *et al.* [15] incorporated Mg into polylactic acid (PLA) composites to produce filaments for the fused deposition modelling (FDM) 3DP process. They assessed how incorporating Mg influenced the thermal, physicochemical, and printability properties of PLA. The 5 and

Table 1: A comparative analysis of 3D-printed Mg-polymer scaffolds

Materials	Manufacturing technique	Advantages	Disadvantages	Ref.
Mg–CS/PCL	Extrusion-based AM	Enhanced bone regeneration; biocompatible with hMSCs	Limited control over microstructure; relatively low resolution	[54]
Mg powder	Room-temp extrusion	Porous Mg scaffold with hierarchical pores and high porosity	No polymer matrix; thermal/mechanical properties not optimized	[55]
Mg/PLA composites	FDM	Printable filaments; Improved thermal and mechanical properties	Lower resolution, rough surface finish typical of FDM	[15]
Gelatin/MgP scaffold	Paste extruding deposition	Optimized printing temperature (25°C) for sol-gel transition <6 wt% gelatin enhanced compressive strength about 16.7 ± 1.9 MPa Improved cell affinity and drug (lysozyme) release control	Limited control over gelatin content and its potential impact on structural homogeneity and long-term stability	[53]

10 wt% Mg filaments were printable and showed potential as biomaterials for 3D-printed bone implants. Similarly, He *et al.* [57] investigated the potential of magnesium oxide (MgO) as a pH-neutralizing agent for glass fibers, whose acidic degradation can impair cell viability and osteogenesis. The findings indicate that MgO serves as a neutralizing agent that effectively prevents the degradation of PGF in acidic environments. As a result, the composite scaffold of (MgO + PGF)/PLA shows considerable promise for applications in bone tissue engineering (BTE). Table 1 shows a comparative analysis of 3D-printed Mg-polymer scaffolds.

SLA, being a more sophisticated process than FDM, has been utilized relatively infrequently for manufacturing polymer composite scaffolds because of the instability of the resin-particle formulation, sedimentation of particles, and post-processing steps [46]. However, the higher resolution of the SLA process can contribute significantly toward more robust and patient-specific implants with higher resolution. One limitation of the SLA process is the range of materials that can be used, as it relies on photopolymerization, which limits the types of polymers that can undergo the required curing process [41]. Additionally, for biomedical applications, material biocompatibility is a critical factor. Poly(methyl methacrylate) (PMMA) has emerged as an ideal candidate due to its proven biocompatibility [58,59], exceptional optical properties, long-term mechanical stability, and ease of processing [60]. PMMA is widely utilized in applications such as bone cement, intraocular lenses, artificial corneal implants, and bone substitutes [59,61]. Its compatibility with SLA for scaffold fabrication allows precise control over structure and mechanical properties, which is essential for optimizing bone substitute effectiveness. These attributes, combined with PMMA's ability to be customized for specific biomedical needs, make it an invaluable material for orthopedic tissue engineering, offering a well-rounded balance of ease of fabrication, performance, and cost-effectiveness [62,63].

Therefore, this study aims to synthesize Mg-incorporated PMMA resin composites with high Mg content for SLA 3DP, specifically targeting biomedical applications such as tissue engineering and drug delivery systems. The photocurable PMMA resin was mixed with high concentrations (wt%) of Mg alloy and then subjected to 3DP and photocuring to evaluate their printability and optimization effects on resulting structures. Physicochemical analysis and biocompatibility tests were performed to assess how the incorporation of Mg affected structural integrity, thermal degradation rate, and biological response in implants. Additionally, obstacles were identified in developing Mg-polymer composites and prospects for these materials.

2 Materials and methods

2.1 Materials

Photocurable PMMA Resin (Bio-Med) was purchased from FromLabs (USA). Magnesium alloy (WE45) particles, with an average diameter ranging from 15 to 53 µm, were supplied by Nanografi Nanotechnology (Turkey). Dimethyl sulfoxide (DMSO) with 99.5% purity and 90% purity isopropyl alcohol were purchased from Sigma-Aldrich.

2.2 Synthesis of magnesium scaffolds

PMMA resin/Mg solutions were prepared by mixing varying amounts (0.5 and 1% by wt) of Mg powder into 10 g of the surfactant DMSO and magnetically stirred for 30 min at 550 rpm. DMSO was used to maintain a uniform distribution of the Mg particles within the PMMA resin matrix, stabilizing the suspension for up to 4 h, sufficient for the SLA printing process. The prepared Mg-DMSO solution was then added to the PMMA resin to formulate composite solutions with 0.5 and 1.0% magnesium concentrations, corresponding to 0.5 g of Mg in 99.5 g of resin and 1.0 g of Mg in 99 g of resin. To achieve the homogeneous solution of PMMA resin/Mg, the mixtures were then mechanically stirred for 12 h at 27°C and 650 rpm. Table 2 reports the composition of the PMMA resin/Mg composite solutions.

2.3 Stability of magnesium-incorporated PMMA resin

To assess the stability of the PMMA resin/Mg composites, samples were stored in the dark at room temperature, and their physical characteristics were observed at intervals of 0, 2, 4, and 8 h post-stirring. The sedimentation of Mg particles over time served as an indicator of the stability of PMMA resin/Mg suspensions.

Table 2: Composition of PMMA resin/Mg solutions

Composition	Magnesium (g)	Surfactant	Resin (g)
PMMA resin		10 g	100
PMMA resin/0.5% Mg	0.5		99.5
PMMA resin/1% Mg	1		99

2.4 3D-printing, optimization, and post-processing

SLA printers employ a standard resin cured within the printer's laser beam wavelength range. However, introducing metal reinforcements into the resin can affect the printer's curing performance, necessitating compatibility with the operational wavelength. This study used an Elegoo Mars 3 printer with a 405 nm wavelength laser. The PMMA resin/Mg solutions were directly transferred to the printer's vat, and various samples were printed. However, adjusting printing parameters for PMMA resin infused with metals is crucial for compatibility. To determine the optimal and stable printing parameters for PMMA resin/Mg scaffolds, tensile testing samples with dimensions of 9.5 mm × 1.6 mm × 57.50 mm were printed using varying exposure times (2.5, 5, 10, and 20 s) and layer heights (0.05, 0.10, 0.15. and 0.2 mm). A total of 16 combinations were tested, and dimensional accuracy was evaluated for each. Based on these results, the optimal printing parameters for the PMMA resin/Mg composites were identified. Following optimization, the composites were then 3D-printed, and then, the samples were washed with 90% isopropyl alcohol and cured with UV light to eliminate residual resin. Refer to Table 3 for the printing parameters employed in sample fabrication.

2.5 Characterization and analysis

The 3D-printed PMMA resin/Mg samples were analyzed for mechanical, thermal, and biomedical characteristics. The morphology of the 3D-printed PMMA resin/Mg composites was examined with a field emission scanning electron microscope (FEI Quanta650FEG) operating at 0.9 cm working distance and 20 kV acceleration voltage. Fourier transform infrared spectroscopy (FTIR) was utilized to examine the chemical structure of the resin solutions. FTIR analysis was conducted with a Nicolet iS50 FT-IR spectrometer (Thermo Scientific, United States) equipped with

Table 3: Printing parameters for SLA AM process

Printing parameters	Value
Exposure time (s)	2.5, 5, 10, 20
Layer height (mm)	0.05, 0.10, 0.15, 0.2
Bottom exposure time (s)	50
Lifting speed (mm/min)	60
Bottom layer count	50

an attenuated total reflectance sampling accessory featuring a diamond crystal plate. Each sample had 32 scans in the FTIR analysis, which had a high spectral resolution of 4 cm^{-1} and covered the spectrum range of 400–4,000 cm^{-1}. The thermal stability of the PMMA resin/Mg composites was evaluated *via* thermogravimetric analysis (TGA) using the Thermal Analyzer (SDT 650, TA Instruments, United States). Samples were heated in a ceramic crucible from room temperature to 500°C at 10°C/min under a nitrogen atmosphere. Differential scanning calorimetry (DSC) was employed to determine cold crystallization, melting point, and decomposition temperature. Tensile stress and Young modulus were measured for each sample using a Mark-10 tensile testing machine (Mark-10 Corporation, USA) and then plotted to determine the mechanical properties. A gauge length of 30 mm and a crosshead speed of 2.1 mm/min were used for the experiments. The tensile strength was ascertained by applying a uniaxial force until the sample fractured. Meanwhile, the Young's modulus was determined from the stress–strain curve obtained during the tensile test, reflecting the material's stiffness and resistance to deformation under load.

2.6 Cell culture

The cytotoxicity of the polymer-magnesium scaffolds was evaluated using mouse embryonic fibroblasts (MEFs). The cells were cultured in DMEM GlutaMAX™ (Gibco), supplemented with 10% fetal bovine serum, 1% antibiotic–antimycotic solution, and one non-essential amino acid. A total of 2,500 cells were seeded into 48-well plates and incubated for 5 days at 37°C in an atmosphere of 5% CO_2 and 20% O_2. After 5 days, the media was replaced with media containing 10 mm × 10 mm PMMA resin/Mg scaffolds. These scaffolds were pre-incubated in 3 ml of media for at least 5 days before being introduced to the MEFs. The PMMA resin/Mg scaffolds were UV sterilized for 45 min before use.

2.7 Cytotoxicity analysis and quantification

After 72 h of incubation of the MEFs in media containing PMMA resin/Mg scaffolds, cell viability was assessed using a 0.2% crystal violet assay. The wells were washed with 1× phosphate-buffered solution (PBS) and treated with 0.2% crystal violet for 30 min, followed by 45-min 1× PBS washes. After allowing the plate to air dry, the iBright1500 imaging system (Invitrogen) was used to image the plates the next day. FIJI-ImageJ software was used to analyze the images. Threshold images were generated from TIFF files, and the ROI manager was utilized to quantify stain intensity within the wells. Statistical analysis was conducted using GraphPad Prism software, with *P*-values calculated using an unpaired *t*-test.

2.8 Cell adhesion

The scaffolds with different concentrations of Mg were UV sterilized for 45 min. The scaffolds were then placed into 12-well plates, and media droplets containing 30,000 cells were seeded onto each scaffold. The plates were incubated for 1 h to allow for cell adhesion. After 1 h, the media volume was increased to 1 mL. A media change was performed every 2 days. The scaffolds were examined after 8 days of incubation using the live cell nuclear probe NucBlue™ (Hoechst 33342) from Invitrogen™ (catalogue No. R37605). The scaffolds were then imaged using an Evos fluorescence imaging microscope.

3 Results and discussion

3.1 Stability of PMMA resin/Mg suspension

PMMA resin solutions containing Mg were stored in the dark and examined for physical changes at 0, 2, 4, and 8 h post-stirring. The PMMA resin/0.5% Mg and PMMA resin/1% Mg remained stable for up to 4 h. However, the sedimentation of the particles was easily observable after 3 h, and after around 7 and 8 h, the particles had completely settled at the bottom. The PMMA resin solutions remained stable for up to four hours when left undisturbed in the dark. However, after this duration, the particles began to settle, and by the eighth hour, sedimentation of particles at the bottom was noticeable. Figure 1 shows the stability of the 1% concentration resin solution.

3.2 Optimization of magnesium-incorporated PMMA resin

The optimal printing parameters for the PMMA resin/Mg composites were identified through a systematic evaluation of 16 combinations of exposure times and layer height. The results revealed that samples printed with a 0.05 mm layer height and 10 s exposure time (OP3) exhibited high dimensional precision with a length of 58.26 mm, a width

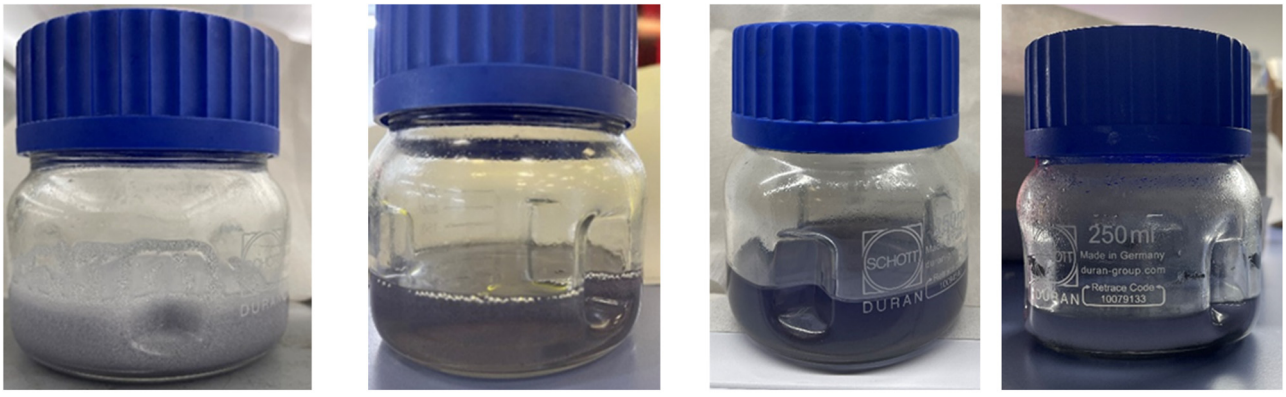

Figure 1: PMMA resin/1% Mg: (a) after stirring, (b) after 2 h, (c) after 4 h, and (d) after 8 h.

of 10.02 ± 0.04 mm, and a thickness of 1.58 ± 0.02 mm, closely matching the intended design. While other combinations, such as OP6 and OP7 (0.1 mm layer height with 10 and 20 s exposure), also showed good dimensional accuracy, they slightly deviated in consistency and over-cured at higher exposure times, which affects feature resolution and mechanical performance. Table 4 illustrates the dimensional assessment data for the optimization study of PMMA resin/Mg scaffolds.

3.3 3D printing and post-processing

The PMMA resin/Mg composite samples were 3D-printed after optimizing the UV light exposure time and the layer height during printing. Various shapes were printed for each sample depending on the type of characterization tests to be performed. Dumbbell-shaped specimens used for tensile testing are shown in Figure 2. After printing, the samples were placed in isopropyl alcohol for 10 min and then exposed to UV light for another 10 min to remove any uncured resin.

3.4 Scanning electron microscope (SEM)

A cross-sectional SEM study was conducted to examine the distribution of Mg particles within the PMMA resin in the composites, designated as PMMA resin/0.5% Mg and PMMA resin/1% Mg. The examination aimed to determine Mg's spatial arrangement and dispersion in the PMMA resin after 3DP. As shown in Figure 3, the cross-sectional image

Table 4: The dimensional data for the optimization study of PMMA resin/Mg composites

Sample	Layer height (mm)	Exposure time (s)	Length (mm)	Width (mm)	Thickness (mm)
OP1	0.05	2.5	57.45	9.73 ± 0.04	0.65 ± 0.03
OP2	0.05	5	58.32	9.92 ± 0.05	1.41 ± 0.04
OP3	0.05	10	58.26	10.02 ± 0.04	1.58 ± 0.02
OP4	0.05	20	58.60	9.82 ± 0.03	1.52 ± 0.05
OP5	0.1	2.5	58.68	10.20 ± 0.02	1.49 ± 0.02
OP6	0.1	5	58.44	10.03 ± 0.02	1.58 ± 0.03
OP7	0.1	10	58.57	10.06 ± 0.07	1.71 ± 0.04
OP8	0.1	20	58.63	10.24 ± 0.05	1.71 ± 0.04
OP9	0.15	2.5	58.04	9.95 ± 0.05	1.73 ± 0.08
OP10	0.15	5	58.27	9.95 ± 0.05	1.79 ± 0.03
OP11	0.15	10	58.12	9.88 ± 0.02	1.67 ± 0.04
OP12	0.15	20	58.83	9.99 ± 0.03	1.60 ± 0.01
OP13	0.2	2.5	58.15	9.72 ± 0.08	1.53 ± 0.07
OP14	0.2	5	58.23	9.84 ± 0.06	1.39 ± 0.09
OP15	0.2	10	58.38	9.87 ± 0.03	1.47 ± 0.04
OP16	0.2	20	58.05	10.15 ± 0.05	1.53 ± 0.05

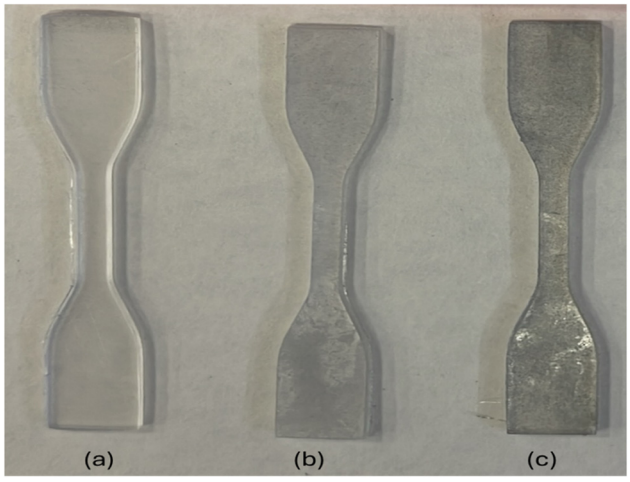

Figure 2: Dumbbell-shaped scaffold: (a) PMMA resin, (b) PMMA resin/0.5% Mg, and (c) PMMA resin/1% Mg.

of the PMMA resin/0.5% Mg sample reveals that the Mg particles are evenly dispersed within the polymer matrix, with no air gaps or cracks present. This uniform distribution is essential for 3DP and significantly impacts the mechanical properties of the scaffold, making it well-suited for creating complex structures.

3.5 Fourier transform infrared

FTIR spectroscopy uses infrared radiation to detect and analyze the chemical functional groups within a material. By analyzing the intensity and position of peaks in the FTIR spectrum, one can determine the abundance of each component, assess interactions between materials, and evaluate the substance's purity. In Figure 4, Mg-containing samples show an increase in the peak, which is related to C–O stretching and is seen between 900 and 1,100 cm^{-1}. However, in PMMA resin, this peak is not discernible. The interaction between the Mg ion and the methoxy group is responsible for this rise [64]. The 1,300 and 1,500 cm^{-1} peaks correspond to C–H_2 bending vibrations. These peaks decrease in samples with 0.5 and 1% Mg concentration, whereas the peak intensity is higher in the pure PMMA resin sample. This suggests that Mg reacts with the polymer, leading to a reduction in these specific vibrational peaks. The peak represents the carboxyl group (C═O) at 1,716 cm^{-1} for the ester group. As the amount of Mg increases, its intensity decreases, suggesting possible breakdown or interaction with other components [65,66]. Peaks ranging from approximately 1,850 to 2,600 cm^{-1} may signify alkyl groups (C═O stretching), aromatic groups, CO_2, or carbonyl groups. These peaks exhibit reduced intensity with the addition of Mg reinforcement. A peak from 2,800 to 3,100 cm^{-1} is observed, which indicates C–H stretching, and its intensity increases with increasing Mg concentration [64,67]. Peaks at 3,651 cm^{-1} correspond to O–H stretching vibration due to moisture absorption, likely caused by uncured resin presence in the 3D-printed parts [68,69].

3.6 Thermogravimetric analysis

TGA was utilized to assess the material's thermal stability, decomposition temperature, and weight loss characteristics under controlled conditions, either over time or at specific temperatures. As illustrated in Figure 5(a), TGA helps identify the temperature at which decomposition starts and evaluates the degradation range of the PMMA resin/Mg composite across various temperatures. This analysis provides insight into how Mg incorporation affects the

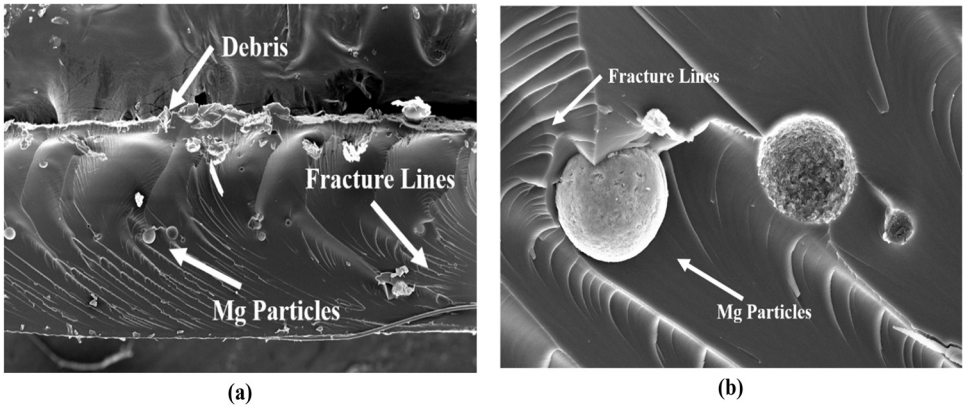

Figure 3: (a) Cross-section of PMMA resin/0.5% Mg sample and (b) Mg-ions in PMMA resin/0.5% Mg sample.

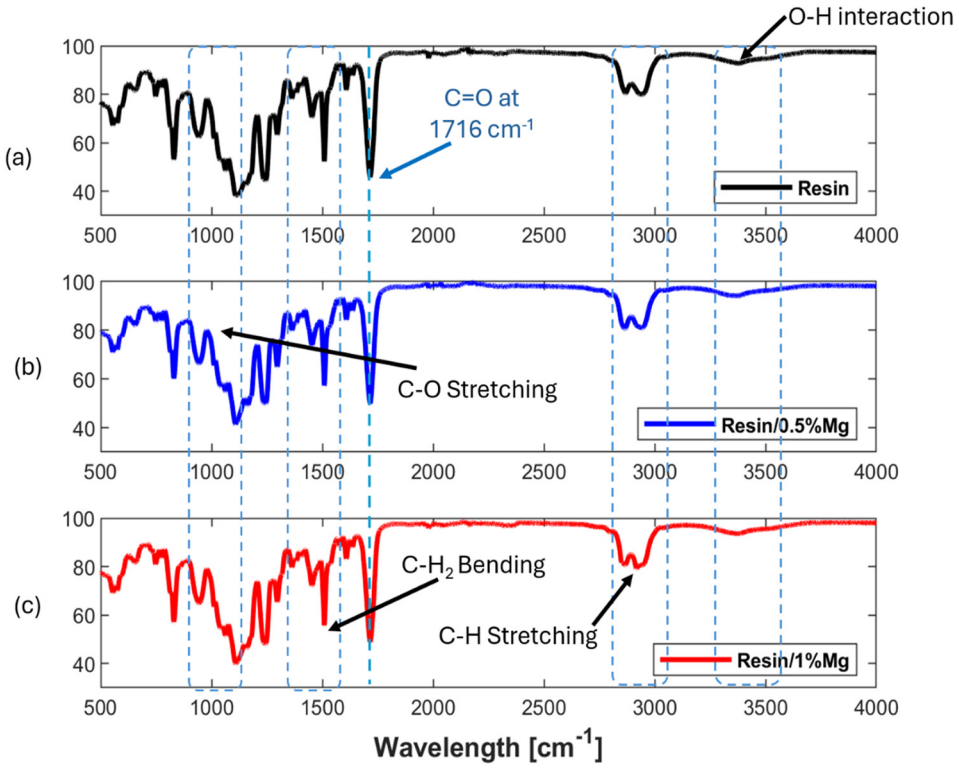

Figure 4: FTIR for samples: (a) PMMA resin, (b) PMMA resin/0.5% Mg, and (c) PMMA resin/1% Mg.

PMMA resin's thermal stability. Initially, the samples show weight loss starting around 50–60°C, likely due to solvent evaporation. It is recommended that a post-treatment involving a heat treatment at 40°C be performed to ensure the elimination of any remaining solvent within the scaffolds. Thermal degradation of the PMMA resin occurs between 320°C and approximately 460°C [70–72]. In contrast, at both concentrations, the PMMA resin/Mg

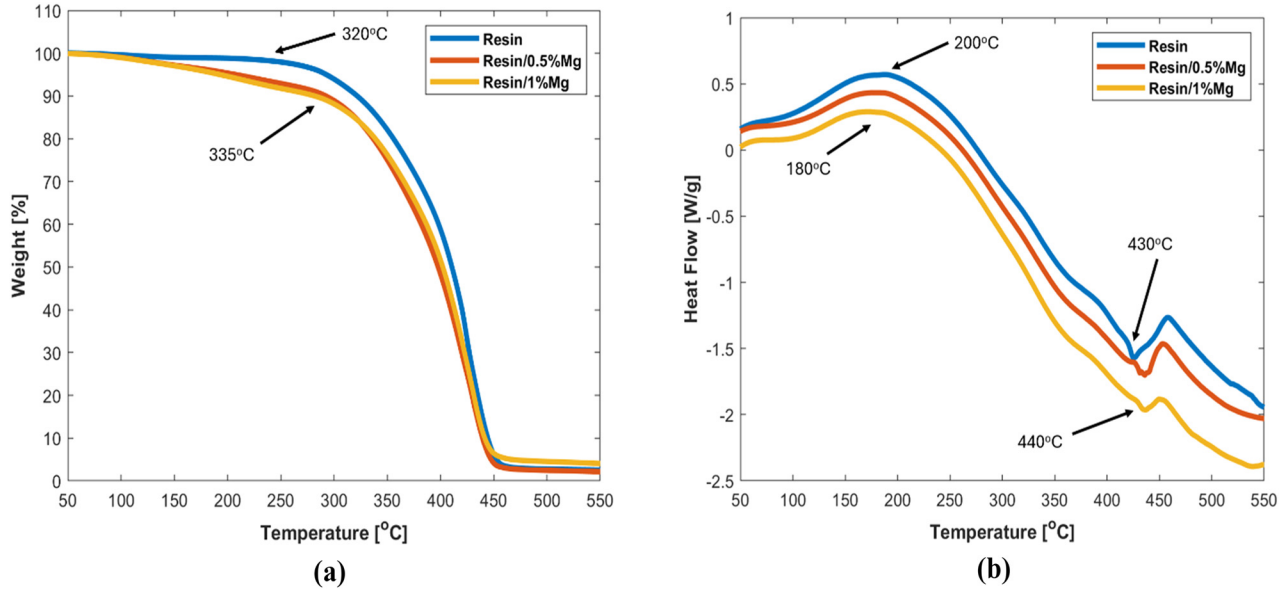

Figure 5: (a) TGA for PMMA resin, PMMA resin/0.5% Mg, and PMMA resin/1% Mg and (b) DSC for PMMA, PMMA resin/0.5% Mg, and PMMA resin/1% Mg.

composite begins degradation around 330°C for the PMMA resin/0.5% Mg sample, whereas 335°C for the PMMA resin/1% Mg sample. This indicates that adding Mg to the PMMA resin shifts the onset of thermal degradation to higher temperatures, suggesting an enhancement in the PMMA resin's thermal stability [73].

Additionally, the TGA results reveal that the incorporation of Mg leads to changes in the degradation profile of the composite, which could imply altered thermal behavior and improved resistance to thermal stress. PMMA resin/Mg composite shows a more gradual weight loss pattern than pure PMMA resin, highlighting its enhanced thermal stability. This information is crucial for applications where high thermal stability is required, as the presence of Mg appears to improve the PMMA resin's performance under elevated temperature conditions.

3.7 Differential scanning calorimetry

DSC is conducted to observe the thermal characteristics of pure PMMA resin and PMMA resin/Mg composite by measuring the difference between the heat flow of the material and the reference. Data on changes in heat capacity, crystallization, phase transitions, melting, glass transitions, and chemical reactions can be obtained from the heat flow differential. The graph and data analysis showed that adding Mg lowers the onset temperature of thermal decomposition, shifting it from approximately 200°C in the pure resin to around 180°C in the resin/1% Mg sample. Mg also reduces the time required for crystallization because it functions as a nucleation agent. Nonetheless, the degree of crystallinity is comparatively stable for polymers incorporating Mg. Figure 5(b) illustrates the DSC for pure PMMA resin, 0.5 and 1% PMMA resin/Mg composite.

3.8 Tensile properties

Tensile strength measures the maximum tensile stress (stretch) a material can withstand before breaking. This mechanical property indicates the material's ability to resist deformation and breaking under tension. Figure 6 shows the mechanical testing machine and a 3D-printed sample during and after the test. The stress-strain graph of PMMA and PMMA resin/Mg helps us determine Young's modulus for each sample. The mechanical characteristics of 3D-printed PMMA resin/Mg composite are given in Table 5. According to the stress-strain curve in Figure 7, Young's modulus decreases as the Mg content in the PMMA resin increases. Pure PMMA resin exhibited the highest ultimate tensile strength (approximately 26 MPa) and stiffness (estimated Young's modulus around 707 MPa). With the addition of Mg, both tensile strength and stiffness decreased, with the 1% Mg composite showing the lowest values (UTS ~19 MPa, estimated Young's modulus ~392 MPa). The PMMA resin/1% Mg has the least surface area under the curve, indicating a reduction in stiffness and making the material ductile compared to the pure PMMA resin.

As illustrated in Figure 7c, the failure strain represents the amount of deformation a material experiences before breaking, offering valuable insight into its ductility or brittleness. Among all the tested samples, pure PMMA resin exhibited the lowest failure strain, indicating its inherently

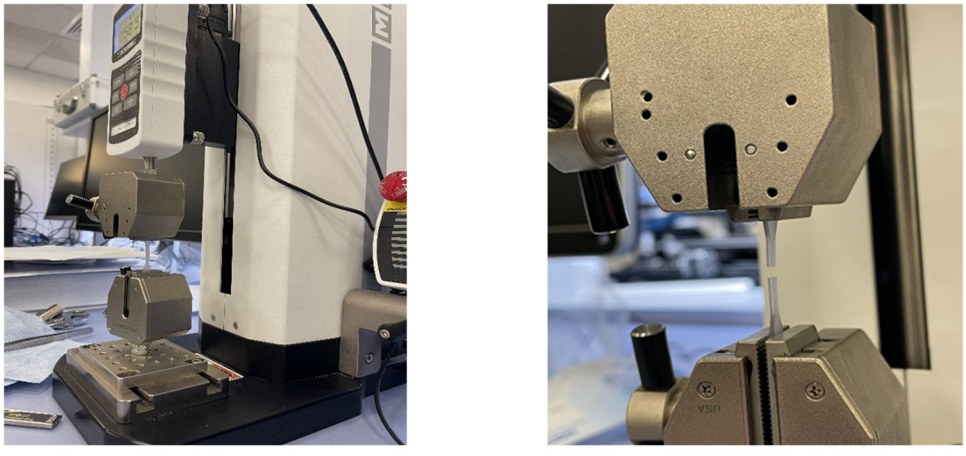

(a) (b)

Figure 6: (a) MARK 10 UTM with the sample for testing and (b) the sample breaks after it reaches the failure strain.

Table 5: Tensile mechanical characteristics of PMMA resin/Mg samples

Samples	Ultimate strength (MPa)	Failure strain (%)	Young's modulus (MPa)
PMMA resin (0%)	26.23 ± 0.14	0.095 ± 0.01	707.81
PMMA resin/0.5% Mg	22.87 ± 0.3	0.12 ± 0.02	419.37
PMMA resin/1% Mg	19.46 ± 0.25	0.115 ± 0.02	392.88

brittle nature. In contrast, incorporating Mg into the PMMA matrix led to a noticeable increase in ductility. The 1% PMMA resin/1% Mg composite reached the highest failure strain of 0.13%, suggesting that Mg enhances the composite's ability to deform before failure. This observation highlights a potential trade-off – as Mg content increases, ductility improves while strength and stiffness may decrease, reflecting a shift in the composite's mechanical performance profile.

3.9 Cell adhesion and cytotoxicity

To evaluate any cytotoxic release by the magnesium, PMMA resin scaffold for biomedical applications and ensure the material's biocompatibility, a 10 mm × 10 mm PMMA resin/Mg scaffold was incubated in media for a period of ≥5 days, allowing any leachable components to diffuse into the media. This conditioned media was subsequently applied to MEFs, and the cytotoxic effects were evaluated after 3 days of exposure. Cytotoxicity tests revealed that the PMMA resin and PMMA resin/Mg composites are not toxic. Additionally, the incorporation of Mg into the PMMA resin did not hinder cell proliferation. Figure 8 shows the cell viability, indicating that the material is safe to use for biomedical applications and has no cytotoxic effect on cells. We next assessed whether these scaffolds supported cell adhesion by seeding 30,000 cells onto them and examining the scaffolds on day 8. After 8 days of incubation, the cells were labeled with a nuclear

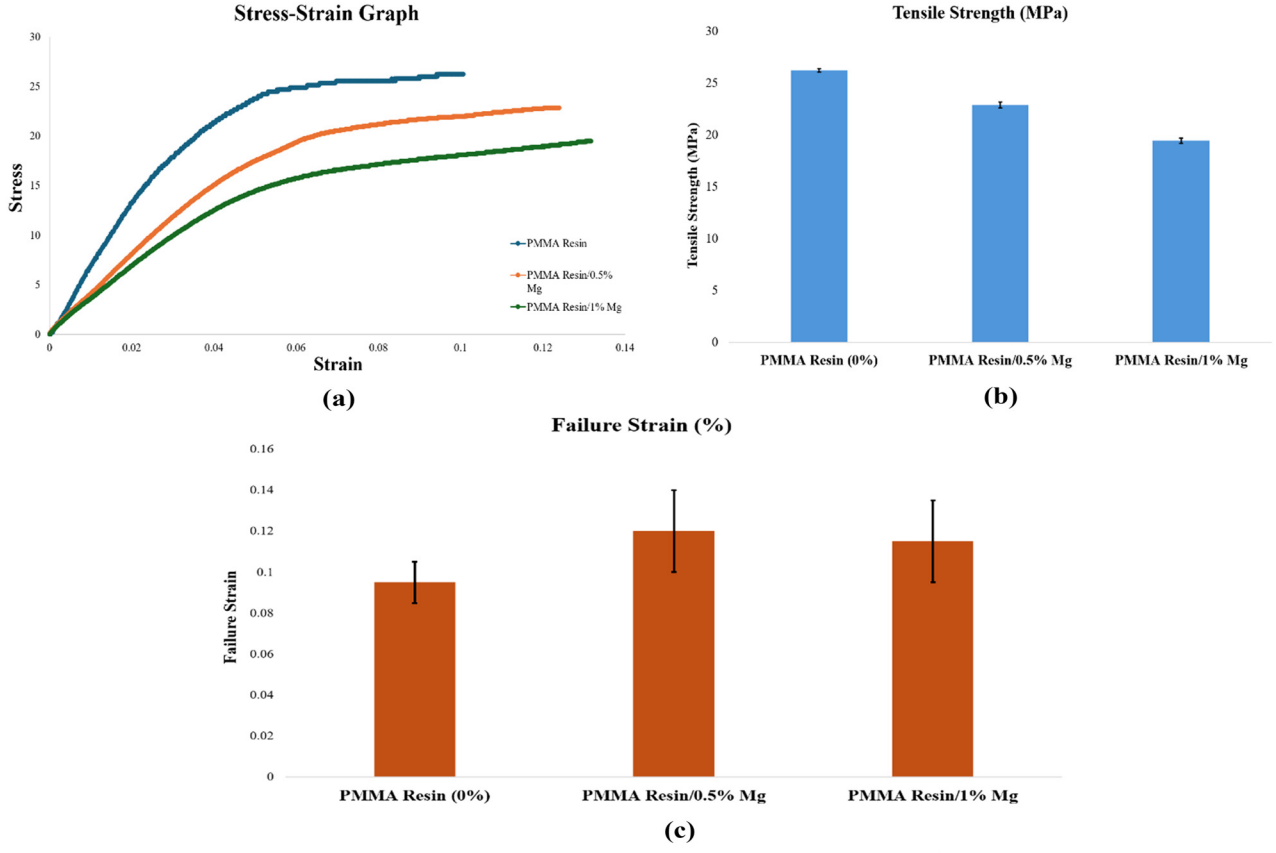

Figure 7: (a) Stress–strain curves, (b) tensile strength, and (c) failure strain for PMMA resin, PMMA resin/0.5% Mg, and PMMA resin/1% Mg.

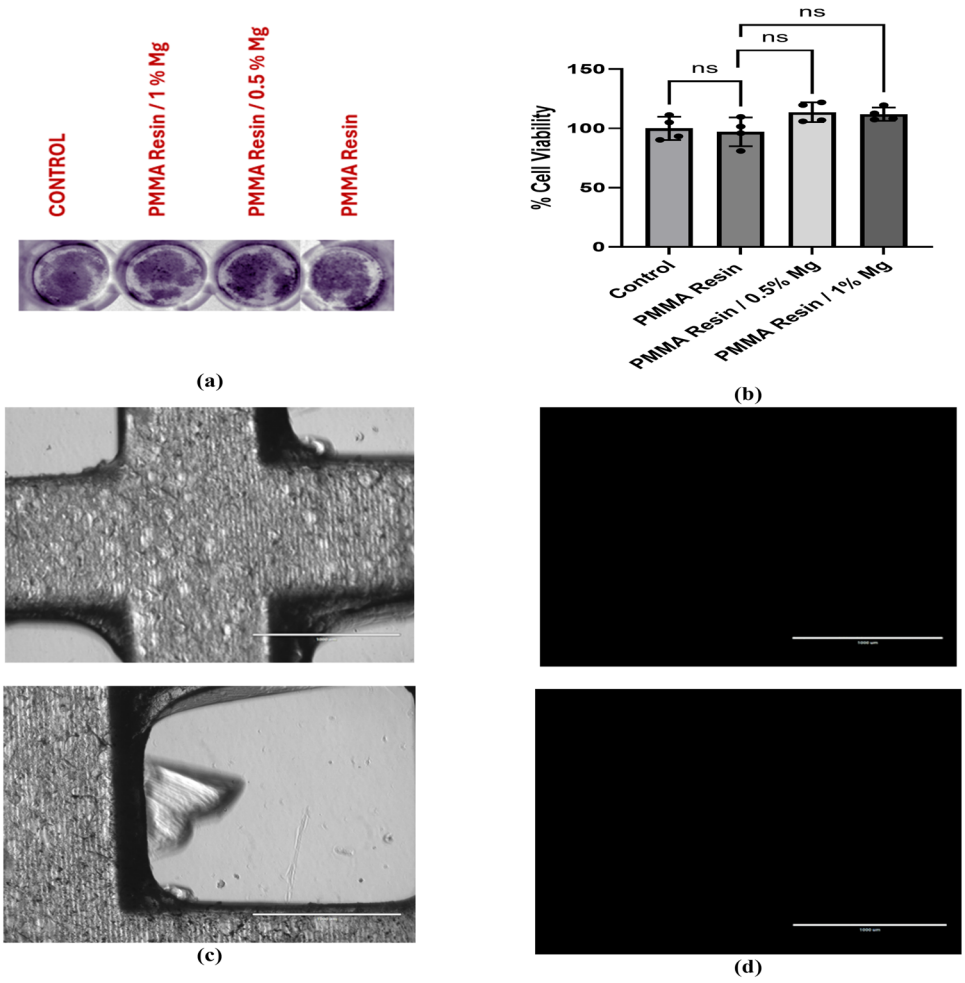

Figure 8: (a) Crystal violet cytotoxicity analysis of MEFs incubated in media containing material released from different scaffolds: PMMA resin, PMMA resin/0.5% Mg scaffold, and PMMA resin/1% Mg scaffold and control media (media not incubated with any scaffold). Crystal violet staining showed no noticeable differences between groups, suggesting equivalent cell viability. (b) Quantification of cytotoxicity, showing the percentage of viable cells after 72 h of incubation with the viability of media containing material released from PMMA resin, PMMA resin/0.5% Mg scaffold, and PMMA resin/1% Mg scaffolds. Quantification of the crystal violet assay showed no significant differences in cell density between the groups. Data presented are of four biological replicates, analyzed by unpaired *t*-tests with a 95% confidence level (ns = not significant). (c) Brightfield images of the PMMA resin with 0% Mg scaffold after cell seeding and 8 days incubation. (d) Fluorescent images of the cells labeled with the live nuclear stain NucBlue™ show no nuclei on the scaffold. Scale bar = 1,000 µm.

stain to identify any adhered cells. No nuclear staining was observed on the scaffold, indicating that no cells adhered to the surface (Figure 8c). This observation was consistent across all scaffolds with different concentrations of Mg (data not shown). This suggests that these scaffolds do not support cell adhesion and, therefore, require modifications to enhance this capability. Figure 8(a) and (b) illustrate the cell viability of PMMA, indicating that the material supports cell viability without being cytotoxic. Figure 8(c) and (d) represent the Brightfield and Fluorescent images of the PMMA resin scaffold after cell seeding and 8 days of incubation, which show no nuclei on the scaffold.

4 Conclusions and future prospects

This study advances ongoing research on the AM of Mg-incorporated composites by synthesizing and characterizing PMMA resin/Mg composite using SLA. The findings demonstrate the feasibility of using SLA to fabricate biocompatible and thermally stable scaffolds from these composite resins, holding promise for applications like wound healing, transdermal drug delivery, and potentially BTE. The incorporation of Mg influences the physicochemical and mechanical behavior of the resin, providing insight into tailoring process parameters and properties for specific biomedical applications. Different concentrations of

Mg were incorporated into the PMMA resin, and the printed scaffolds were subjected to morphological and physicochemical analyses to evaluate the interaction between Mg and the polymer, as well as the impact of Mg addition on thermal degradation. The FTIR analysis has a maximum intensity peak at 1,716 cm^{-1} for pure PMMA resin, while the peak decreases with the addition of Mg, indicating possible interaction within the scaffold. It also showed a high-intensity peak at 3,651 cm^{-1}, the OH component region, most likely caused by the printed part's uncured resin, as indicated in different studies. Mechanical testing revealed that increasing Mg content led to a measurable reduction in tensile strength and stiffness. Pure PMMA resin exhibited the highest ultimate tensile strength at 26.23 ± 0.14 MPa and an elastic modulus of 707.81 MPa. In contrast, PMMA resin/1% Mg showed the lowest strength (19.46 ± 0.25 MPa) and modulus (392.88 MPa), indicating a decrease in mechanical integrity with higher Mg content. However, a slight increase in maximum elongation for the Mg-incorporated samples suggests some improvement in ductility. In the PMMA resin/Mg composite, the onset of thermal degradation occurred at higher temperatures – 320°C for 0.5% Mg and 335°C for 1% Mg – compared to the broader degradation range of pure PMMA, indicating enhanced thermal stability of the composites. However, the produced PMMA resin/Mg suspension was successfully used for 3DP by SLA; challenges arose due to the instability of the PMMA resin particle formulation when magnesium particles settled in the vat, obstructing the laser beam and interfering with the polymerization process. To ensure even distribution of Mg particles in the resin, DMSO was used as a surfactant. It effectively stabilized the suspension for up to 4 h, sufficient for printing samples. DMSO was selected based on its superior performance with the chosen resin formulation compared to other surfactants. The larger Mg particle size, which was in the micrometer range rather than the nanoscale scale, is the potential cause of particle sedimentation. Future studies could investigate using nanosized Mg particles and a detailed sedimentation analysis to enhance long-term stability.

The results of mechanical and cytotoxicity assessments support the potential use of PMMA resin/Mg composite in transdermal drug delivery and wound healing, owing to their biocompatibility, degradability, and physicochemical stability. These metal-reinforced composites are also potential candidates for BTE. However, further studies are required to enhance cell adhesion to the surface of the 3D-printed scaffolds. In this study, we tested a UV-curable gelatin–PMMA mixture to enhance cell adhesion; however, it did not yield improved results, likely due to gelatin leaching from unstable crosslinking. To improve cell adhesion on the scaffold surface, future efforts will investigate several strategies, including chemical modification of gelatin, incorporation of bioactive molecules such as collagen or hydroxyapatite, and scaffold micro-patterning. Furthermore, long-term cell viability, proliferation, and differentiation are critical parameters for evaluating the scaffold's full potential in tissue engineering applications. Although these aspects were beyond the scope of the current study, we recognize them as important directions for future work. In particular, we plan to investigate the scaffold's ability to support lineage-specific differentiation of mesenchymal stem cells to better understand its biomedical applicability. The findings of this study pave the way for future research focused on optimizing particle size, improving resin stability, and enhancing bioactivity to fully realize the potential of these functional scaffolds.

Acknowledgments: The authors acknowledge the contributions of HBKU core labs for the support provided in the characterization of the samples. Open Access funding provided by the Qatar National Library.

Funding information: The authors acknowledge the support of QNRF through project NPRP13S-0126-200172 (Additive Manufacturing of Mg-based Porous Tissue Scaffolds).

Author contributions: Conceptualization, A. Afridi and A. Al Rashid; data curation, A. Afridi, S. N. Kalva, and N. A. Al-Maslamani; formal analysis, A. Afridi, S. N. Kalva, and A. Al Rashid, N. A. Al-Maslamani; investigation, A. Afridi; methodology, A. Afridi; project administration, M. Koc; funding acquisition, M. Koc; resources, N. A. Al-Maslamani and M. Koc; supervision, A. Al Rashid, N. A. Al-Maslamani, and M. Koc; validation, A. Afridi, S. N. Kalva, A. Al Rashid, and N. A. Al-Maslamani; visualization, A. Afridi, S. N. Kalva, and A. Al Rashid; writing – original draft, A. Afridi; and writing, review and editing, A. Afridi, S. N. Kalva, A. Al Rashid, N. A. Al-Maslamani, and M. Koç. All authors have accepted responsibility for the entire content of this manuscript and approved its submission.

Conflict of interest: The authors state no conflict of interest.

Data availability statement: The datasets generated and/or analyzed during the current study are available from the corresponding author on reasonable request.

References

[1] Kashirina A, Yao Y, Liu Y, Leng J. Biopolymers as bone substitutes: a review. Biomater Sci. 2019;7:3961–83. doi: 10.1039/C9BM00664H.

[2] Sharma SK, Saxena KK, Malik V, Mohammed KA, Prakash C, Buddhi D, et al. Significance of alloying elements on the mechanical characteristics of Mg-based materials for biomedical applications. Crystals. 2022;12(8):1138. doi: 10.3390/cryst12081138.
[3] Zhang T, Wang W, Liu J, Wang L, Tang Y, Wang K. A review on magnesium alloys for biomedical applications. Front Bioeng Biotechnol. 2022;10:953344. doi: 10.3389/fbioe.2022.953344.
[4] Lee S-J, Kang H-W, Park JK, Rhie J-W, Hahn SK, Cho D-W. Application of microstereolithography in the development of three-dimensional cartilage regeneration scaffolds. Biomed Microdevices. 2008;10:233–41. doi: 10.1007/s10544-007-9129-4.
[5] Cooke MN, Fisher JP, Dean D, Rimnac C, Mikos AG. Use of stereolithography to manufacture critical-sized 3D biodegradable scaffolds for bone ingrowth. J Biomed Mater Res B Appl Biomater. 2003;64B:65–9. doi: 10.1002/jbm.b.10485.
[6] Milovanović J, Stojković M, Trifunović M, Vitković N. Review of bone scaffold design concepts and design methods. Facta Univ, Ser: Mech Eng. 2023;21:151–73.
[7] Koumentakou I, Michopoulou A, Noordam MJ, Terzopoulou Z, Bikiaris DN. 3D-printed scaffolds for tissue engineering applications using thermosensitive hydrogels based on biopolymer blends. J Mater Sci. 2024;59(20):9021–41. doi: 10.1007/s10853-024-09707-0.
[8] Seck TM, Melchels FPW, Feijen J, Grijpma DW. Designed biodegradable hydrogel structures prepared by stereolithography using poly(ethylene glycol)/poly(d,l-lactide)-based resins. J Controlled Release. 2010;148:34–41. doi: 10.1016/j.jconrel.2010.07.111.
[9] Turudija R, Stojković M, Stojković JR, Aranđelović J, Marinković D. Stiffness of anatomically shaped lattice scaffolds made by direct metal laser sintering of Ti-6Al-4V powder: A comparison of two different design variants. Metals. 2024;14:219.
[10] Stojković JR, Stojković M, Turudija R, Aranđelović J, Marinkovic D. Adjustable elasticity of anatomically shaped lattice bone scaffold built by electron beam melting Ti6Al4V powder. Metals. 2023;13:1522.
[11] Badali V, Checa S, Zehn MM, Marinkovic D, Mohammadkhah M. Computational design and evaluation of the mechanical and electrical behavior of a piezoelectric scaffold: a preclinical study. Front Bioeng Biotechnol. 2024;11:1261108. doi: 10.3389/fbioe.2023.1261108.
[12] Muley SV, Vidvans AN, Chaudhari GP, Udainiya S. An assessment of ultra fine grained 316L stainless steel for implant applications. Acta Biomater. 2016;30:408–19. doi: 10.1016/j.actbio.2015.10.043.
[13] Rezaee A, Kermanpur A, Najafizadeh A, Moallemi M. Production of nano/ultrafine grained AISI 201L stainless steel through advanced thermo-mechanical treatment. Mater Sci Eng, A. 2011;528:5025–9. doi: 10.1016/j.msea.2011.02.093.
[14] Xiang DD, Wang P, Tan XP, Chandra S, Wang C, Nai MLS, et al. Anisotropic microstructure and mechanical properties of additively manufactured Co–Cr–Mo alloy using selective electron beam melting for orthopedic implants. Mater Sci Eng, A. 2019;765:138270. doi: 10.1016/j.msea.2019.138270.
[15] Kalva SN, Ali F, Velasquez CA, Koç M. 3D-Printable PLA/Mg composite filaments for potential bone tissue engineering applications. Polymer. 2023;15:2572. doi: 10.3390/polym15112572.
[16] Singh G, Singh S, Prakash C, Ramakrishna S. On investigating the soda-lime shot blasting of AZ31 alloy: Effects on surface roughness, material removal rate, corrosion resistance, and bioactivity. J Magnesium Alloys. 2021;9:1272–84. doi: 10.1016/j.jma.2020.11.017.
[17] Bommala VK, Krishna MG, Rao CT. Magnesium matrix composites for biomedical applications: A review. J Magnesium Alloys. 2019;7:72–9. doi: 10.1016/j.jma.2018.11.001.
[18] Agarwal S, Curtin J, Duffy B, Jaiswal S. Biodegradable magnesium alloys for orthopaedic applications: A review on corrosion, biocompatibility and surface modifications. Mater Sci Eng, C. 2016;68:948–63. doi: 10.1016/j.msec.2016.06.020.
[19] Feng J, Gao C, Safaei B, Qin Z, Wu H, Chu F, et al. Exceptional damping of CFRPs: Unveiling the impact of carbon fiber surface treatments. Composites, Part B. 2025;290:111973. doi: 10.1016/j.compositesb.2024.111973.
[20] Feng J, Li A, Safaei B, Qin Z, Chu F. Revolutionary coatings: Unlocking the full potential of energy dissipation and mechanical properties in nickel foam. Chem Eng J. 2025;505:159461. doi: 10.1016/j.cej.2025.159461.
[21] Francis A, Yang Y, Virtanen S, Boccaccini AR. Iron and iron-based alloys for temporary cardiovascular applications. J Mater Sci Mater Med. 2015;26:138. doi: 10.1007/s10856-015-5473-8.
[22] Wen P, Voshage M, Jauer L, Chen Y, Qin Y, Poprawe R, et al. Laser additive manufacturing of Zn metal parts for biodegradable applications: Processing, formation quality and mechanical properties. Mater Des. 2018;155:36–45. doi: 10.1016/j.matdes.2018.05.057.
[23] Xue D, Yun Y, Tan Z, Dong Z, Schulz MJ. In Vivo and In Vitro degradation behavior of magnesium alloys as biomaterials. J Mater Sci Technol. 2012;28:261–7. doi: 10.1016/S1005-0302(12)60051-6.
[24] Chen Z, Zhang W, Wang M, Backman LJ, Chen J. Effects of zinc, magnesium, and iron ions on bone tissue engineering. ACS Biomater Sci Eng. 2022;8:2321–35. doi: 10.1021/acsbiomaterials.2c00368.
[25] Ali Mohammad A, Mohammadali M, Mahmod K, Khadijeh S. A study of the effect of magnesium hydroxide on the wound healing process in rats. Med J Islamic World Acad Sci. 2006;16:165–70.
[26] Gupta S, Dutta P, Acharya V, Prasad P, Roy A, Bit A. Accelerating skin barrier repair using novel bioactive magnesium-doped nanofibers of non-mulberry silk fibroin during wound healing. J Bioact Compat Polym. 2021;37:38–52. doi: 10.1177/08839115211061737.
[27] Graça A, Bom S, Martins AM, Ribeiro HM, Marto J. Vat-based photopolymerization 3D printing: from materials to topical and transdermal applications. Asian J Pharm Sci. 2024;19(4):100940. doi: 10.1016/j.ajps.2024.100940.
[28] Goyanes A, Det-Amornrat U, Wang J, Basit AW, Gaisford S. 3D scanning and 3D printing as innovative technologies for fabricating personalized topical drug delivery systems. J Controlled Release. 2016;234:41–8. doi: 10.1016/j.jconrel.2016.05.034.
[29] Chen G, Xu Y, Chi Lip Kwok P, Kang L. Pharmaceutical applications of 3D printing. Addit Manuf. 2020;34:101209. doi: 10.1016/j.addma.2020.101209.
[30] Bom S, Martins AM, Ribeiro HM, Marto J. Diving into 3D (bio) printing: A revolutionary tool to customize the production of drug and cell-based systems for skin delivery. Int J Pharm. 2021;605:120794. doi: 10.1016/j.ijpharm.2021.120794.
[31] Moulton SE, Wallace GG. 3-dimensional (3D) fabricated polymer based drug delivery systems. J Controlled Release. 2014;193:27–34. doi: 10.1016/j.jconrel.2014.07.005.
[32] Perez-Valle A, Del Amo C, Andia I. Overview of current advances in extrusion bioprinting for skin applications. Int J Mol Sci. 2020;21:6679. doi: 10.3390/ijms21186679.

[33] He P, Zhao J, Zhang J, Li B, Gou Z, Gou M, et al. Bioprinting of skin constructs for wound healing. Burn Trauma. 2018;6:5. doi: 10.1186/s41038-017-0104-x.
[34] Bom S, Martins AM, Ribeiro HM, Marto J. Diving into 3D (bio) printing: A revolutionary tool to customize the production of drug and cell-based systems for skin delivery. Int J Pharm. 2021;605:120794. doi: 10.1016/j.ijpharm.2021.120794.
[35] Bird D, Ravindra NM. Transdermal drug delivery and patches—An overview. Med Devices Sens. 2020;3:e10069. doi: 10.1002/mds3.10069.
[36] Lee V, Singh G, Trasatti JP, Bjornsson C, Xu X, Tran TN, et al. Design and fabrication of human skin by three-dimensional bioprinting. Tissue Eng, Part C. 2013;20:473–84. doi: 10.1089/ten.tec.2013.0335.
[37] Al-Nimry SS, Daghmash RM. Three dimensional printing and its applications focusing on microneedles for drug delivery. Pharmaceutics. 2023;15:1597. doi: 10.3390/pharmaceutics15061597.
[38] Bártolo P. Stereolithography: materials, processes and applications. Springer Science & Business Media; 2011. p. 1–36. doi: 10.1007/978-0-387-92904-0.
[39] Huang J, Qin Q, Wang J. A review of stereolithography: processes and systems. Processes. 2020;8:1138. doi: 10.3390/pr8091138.
[40] Oliaei SNB. Stereolithography and its applications. Addit Subtract Manuf. 2020;1:229–50.
[41] Afridi A, Al Rashid A, Koç M. Recent advances in the development of stereolithography-based additive manufacturing processes: A review of applications and challenges. Bioprinting. 2024;43:e00360. doi: 10.1016/j.bprint.2024.e00360.
[42] Schmidleithner C, Kalaskar DM. Stereolithography. In: Cvetković D, editor. 3D Printing. Rijeka: IntechOpen; 2018. doi: 10.5772/intechopen.78147.
[43] Manapat JZ, Chen Q, Ye P, Advincula RC. 3D printing of polymer nanocomposites via stereolithography. Macromol Mater Eng. 2017;302:1600553. doi: 10.1002/MAME.201600553.
[44] Ngo TD, Kashani A, Imbalzano G, Nguyen KTQ, Hui D. Additive manufacturing (3D printing): A review of materials, methods, applications and challenges. Composites, Part B. 2018;143:172–96. doi: 10.1016/j.compositesb.2018.02.012.
[45] Robles Martinez P, Basit A, Gaisford S. The history, developments and opportunities of stereolithography. In: Basit AW, Gaisford S. editors. 3D Printing of Pharmaceuticals. 1st edn Cham: Springer; 2018. pp. 55–79. doi: 10.1007/978-3-319-90755-0_4.
[46] Wang X, Jiang M, Zhou Z, Gou J, Hui D. 3D printing of polymer matrix composites: A review and prospective. Composites, Part B. 2017;110:442–58. doi: 10.1016/j.compositesb.2016.11.034.
[47] Melchels FPW, Feijen J, Grijpma DW. A review on stereolithography and its applications in biomedical engineering. Biomaterials. 2010;31:6121–30. doi: 10.1016/j.biomaterials.2010.04.050.
[48] Wang J, Goyanes A, Gaisford S, Basit AW. Stereolithographic (SLA) 3D printing of oral modified-release dosage forms. Int J Pharm. 2016;503:207–12. doi: 10.1016/j.ijpharm.2016.03.016.
[49] Wildemann B, Sander A, Schwabe P, Lucke M, Stöckle U, Raschke M, et al. Short term in vivo biocompatibility testing of biodegradable poly (D,L-lactide)—growth factor coating for orthopaedic implants. Biomaterials. 2005;26:4035–40. doi: 10.1016/j.biomaterials.2004.10.004.
[50] Rahman M, Li Y, Wen C. Realization and characterization of double-layer Ca-P coating on WE43 Mg alloy for biomedical applications. Surf Coat Technol. 2020;398:126091. doi: 10.1016/j.surfcoat.2020.126091.
[51] Ali F, Kalva SN, Koç M. Additive manufacturing of polymer/Mg-based composites for porous tissue scaffolds. Polymers. 2022;14(24):5460. doi: 10.3390/polym14245460.
[52] Ali F, Al Rashid A, Kalva SN, Koç M. Mg-doped PLA composite as a potential material for tissue engineering—synthesis, characterization, and additive manufacturing. Materials. 2023;16:6506. doi: 10.3390/ma16196506.
[53] Farag MM, Yun H. Effect of gelatin addition on fabrication of magnesium phosphate-based scaffolds prepared by additive manufacturing system. Mater Lett. 2014;132:111–5. doi: 10.1016/j.matlet.2014.06.055.
[54] Tsai K-Y, Lin H-Y, Chen Y-W, Lin C-Y, Hsu T-T, Kao C-T. Laser sintered magnesium-calcium silicate/poly-ε-caprolactone scaffold for bone tissue engineering. Materials. 2017;10:65. doi: 10.3390/ma10010065.
[55] Dong J, Li Y, Lin P, Leeflang MA, van Asperen S, Yu K, et al. Solvent-cast 3D printing of magnesium scaffolds. Acta Biomater. 2020;114:497–514. doi: 10.1016/j.actbio.2020.08.002.
[56] Lin T, Wang X, Jin L, Li W, Zhang Y, Wang A, et al. Manufacturing of porous magnesium scaffolds for bone tissue engineering by 3D gel-printing. Mater Des. 2021;209:109948. doi: 10.1016/j.matdes.2021.109948.
[57] He L, Liu X, Rudd C. Additive-manufactured gyroid scaffolds of magnesium oxide, phosphate glass fiber and polylactic acid composite for bone tissue engineering. Polymers. 2021;13(2):270. doi: 10.3390/polym13020270.
[58] Ramanathan S, Lin Y-C, Thirumurugan S, Hu C-C, Duann Y-F, Chung R-J. Poly(methyl methacrylate) in orthopedics: strategies, challenges, and prospects in bone tissue engineering. Polymer. 2024;16(3):367. doi: 10.3390/polym16030367.
[59] Chen N. Embedded 3D printing and pressurized thermo-curing of PMMA for medical implants. J Mech Behav Biomed Mater. 2023;146:106083. doi: 10.1016/j.jmbbm.2023.106083.
[60] Amirabad LM, Tahriri M, Zarrintaj P, Ghaffari R, Tayebi L. Preparation and characterization of TiO2-coated polymerization of methyl methacrylate (PMMA) for biomedical applications: In vitro study. Asia-Pac J Chem Eng. 2022;17:e2761. doi: 10.1002/apj.2761.
[61] Marin E, Mukai M, Boschetto F, Sunthar TPM, Adachi T, Zhu W, et al. Production of antibacterial PMMA-based composites through stereolithography. Mater Today Commun. 2022;32:103943. doi: 10.1016/j.mtcomm.2022.103943.
[62] Feuser PE, Gaspar PC, Ricci-Júnior E, da Silva MCS, Nele M, Sayer C, et al. Synthesis and characterization of poly(Methyl Methacrylate) PMMA and evaluation of cytotoxicity for biomedical application. Macromol Symp. 2014;343:65–9. doi: 10.1002/masy.201300194.
[63] Saxena P, Shukla P. A comparative analysis of the basic properties and applications of poly (vinylidene fluoride) (PVDF) and poly (methyl methacrylate) (PMMA). Polym Bull. 2022;79:5635–65. doi: 10.1007/s00289-021-03790-y.
[64] Shen C, Aguey-Zinsou K-F. Can γ-MgH2 improve the hydrogen storage properties of magnesium? J Mater Chem A. 2017;5:8644–52. doi: 10.1039/C7TA01724C.
[65] Sun Y, Shen C, Lai Q, Liu W, Wang D-W, Aguey-Zinsou K-F. Tailoring magnesium based materials for hydrogen storage through synthesis: Current state of the art. Energy Storage Mater. 2018;10:168–98. doi: 10.1016/j.ensm.2017.01.010.
[66] Hemraj-Benny T, Pigza JA, Budhoo S, Condon L, Depner SW, Dennis RV, et al. Synthesis of novel single-walled carbon nanotube—magnesium nanoparticle composites by a solution reduction method. Mater Lett. 2014;117:305–8. doi: 10.1016/j.matlet.2013.12.032.
[67] Grubbs RB. Roles of polymer ligands in nanoparticle stabilization. Polym Rev. 2007;47:197–215. doi: 10.1080/15583720701271245.

[68] Darman Singho N, Johan M, Che Lah N. Temperature-dependent properties of silver-poly(methylmethacrylate) nanocomposites synthesized by in-situ technique. Nanoscale Res Lett. 2014;9:42. doi: 10.1186/1556-276X-9-42.
[69] Sun Y, Shen C, Lai Q, Liu W, Wang D-W, Aguey-Zinsou F. Tailoring magnesium based materials for hydrogen storage through synthesis: Current state of the art. Energy Storage Mater. 2018;10:168–98. doi: 10.1016/j.ensm.2017.01.010.
[70] Hafizah NN, Mamat MH, Said CMS, Abidin MH, Rusop M. Thermal degradation of nanocomposited PMMA/TiO2 nanocomposites. IOP Conf Ser: Mater Sci Eng. 2013;46:012045. doi: 10.1088/1757-899X/46/1/012045.
[71] Saladino ML, Motaung TE, Luyt AS, Spinella A, Nasillo G, Caponetti E. The effect of silica nanoparticles on the morphology, mechanical properties and thermal degradation kinetics of PMMA. Polym Degrad Stab. 2012;97:452–9. doi: 10.1016/j.polymdegradstab.2011.11.006.
[72] Motaung TE, Luyt AS, Bondioli F, Messori M, Saladino ML, Spinella A, et al. PMMA–titania nanocomposites: Properties and thermal degradation behaviour. Polym Degrad Stab. 2012;97:1325–33. doi: 10.1016/j.polymdegradstab.2012.05.022.
[73] Liang H, Chen D, Chen M, Li W, Snyders R. Study of the synthesis of PMMA-Mg nanocomposite for hydrogen storage application. Int J Hydrogen Energy. 2020;45:4743–53. doi: 10.1016/j.ijhydene.2019.12.039.